BIOPHYSICS

Spatial organization of protein aggregates on red blood cells as physical biomarkers of Alzheimer's disease pathology

Peter Niraj Nirmalraj[1]*, Thomas Schneider[2], Ansgar Felbecker[2]*

Quantifying physical differences of protein aggregates implicated in Alzheimer's disease (AD), in blood, could provide crucial information on disease stages. Here, red blood cells (RBCs) from 50 patients with neurocognitive complaints and 16 healthy individuals were profiled using an atomic force microscope (AFM). AFM measurements revealed patient age– and stage of neurocognitive disorder–dependent differences in size, shape, morphology, assembly, and prevalence of protein aggregates on RBCs, referred to as physical biomarkers. Crystals composed of fibrils were exclusively detected on RBCs for AD patients aged above 80 years. Fibril prevalence was negatively correlated with the cerebrospinal fluid (CSF) β-amyloid (Aβ) 42/40 ratio and was observed to be higher in the Aβ-positive patient category. Using a cutoff of ≥40% fibril prevalence, the CSF Aβ status was classified with 88% accuracy (sensitivity 100%, specificity 73%). The merits and challenges in integrating physical biomarkers in AD diagnosis are discussed.

INTRODUCTION

Alzheimer's disease (AD) is a progressive neurodegenerative disorder in which the pathophysiological processes can be triggered nearly 20 years (*1*) before the decline in memory and cognitive abilities becomes noticeable. Early signs of AD range from difficulties in finishing usual tasks, struggling with vocabulary, losing things more often, increased anxiety, loss of insight, withdrawal from social life, to confusion in time and place. Currently, 40 million people suffer from AD globally, and numbers are estimated to triple by 2050 (*2*), which could be an underestimate as they do not include individuals at the very early stages of the disease. The misfolding and abnormal aggregation of β-amyloid (Aβ) and tau proteins in the brain is considered to be the pathological hallmarks (*3*, *4*) of AD. The early identification of individuals with this pathology is crucial for a successful treatment that can slow AD progression using existing behavioral and lifestyle changes as well as future chemo- and immunotherapies. At present, measurements of Aβ (isoforms Aβ40 and Aβ42 and the Aβ42/40 ratio) and tau protein (total tau and phospho-tau 181 and 217) levels in the cerebrospinal fluid (CSF) (*5*) and amyloid–positron emission tomography (PET) scans (*6*) are the gold standards in the clinical detection of AD pathology (*7*, *8*). Recently developed immunoassays can also detect amyloid (*9*, *10*) and tau (*11*–*13*) isoforms in blood serum, and risk prediction models (*14*) have been shown to achieve a patient-specific prognosis of cognitive decline in patients with mild cognitive impairment using plasma biomarkers of Aβ and tau proteins. A recent review on using Aβ and tau as fluid biomarkers in the diagnosis of AD by Lee *et al.* (*15*) summarizes the advantages and limitations of protein analytics in CSF. Merits range from the fact that CSF extraction does not involve radioactivity and is lower in cost compared to brain scans. Nonetheless, challenges, such as the requirement of lumbar puncture decreased levels of Aβ42 in CSF due to their deposition in the brain as plaques and the increased CSF t-tau levels due to other acute disorders (*16*), remain. In contrast, screening blood plasma (*17*–*19*) for Aβ is less invasive compared to CSF analytics, but this medium also hosts numerous other pathological and nonpathological proteins in plasma (*15*). Hence, precise quantification is challenging, but their diagnostic accuracy is under evaluation as they hold the promise to allow for an inexpensive and minimally invasive method of testing. In general, biomarker-guided methods can quantify the total Aβ40, Aβ42, p-tau, and t-tau in CSF, blood plasma, and serum. However, elemental information on the morphological and size differences of the pathological protein aggregates present within body fluids, which could also shed light on the disease stage, remains largely unavailable to the clinicians.

Conversely, the research topic of Aβ and tau isoforms to bind to red blood cells (RBCs) (*20*, *21*) has received much lesser attention compared to efforts in quantifying CSF, plasma-Aβ, and tau in CSF and blood plasma. With ~500 ml of CSF being cleared daily into the bloodstream and taken together with emerging evidence that Aβ and tau levels increase in blood after crossing the blood-brain barrier (*22*, *23*), there is a higher propensity for these pathological protein aggregates to interface and adhere on RBCs. If this hypothesis can be verified with high spatial clarity and evidence that pathological proteins adsorb on RBCs, then the surface of RBCs could be considered as an additional source for screening proteins implicated in AD pathology. Atomic force microscopy (AFM) is one such analytical technique that has been demonstrated to be a promising tool in biomedical research ranging from cancer diagnosis (*24*) to early detection of osteoarthritis (*25*). The advantages of the high-resolution imaging capability of the AFM has also been exploited toward resolving transient protein nanostructures occurring along the aggregation pathway of Aβ40 (*26*, *27*), Aβ42 (*26*, *28*, *29*), and tau proteins (*30*, *31*) prepared in solutions at physiological concentrations (*26*–*28*, *30*, *32*) and deposited on solid surfaces for imaging. Furthermore, AFM has also been used to assess the health of RBCs (*33*–*35*) and hematopathology (*33*, *34*, *36*) by monitoring nanoscopic changes in RBC topology. More recently,

[1]Transport at Nanoscale Interfaces Laboratory, Swiss Federal Laboratories for Materials Science and Technology, Dübendorf CH-8600, Switzerland. [2]Department of Neurology, Cantonal Hospital St. Gallen, St. Gallen CH-9007, Switzerland.
*Corresponding author. Email: peter.nirmalraj@empa.ch (P.N.N.); ansgar.felbecker@kssg.ch (A.F.)

it has been reported that soluble Aβ protein aggregates deposited on smooth solid surfaces could be characterized using AFM in CSF extracted from patients with AD (*37*, *38*). The viscosity of the whole blood in a wet state, variations in surface corrugations of an air-dried blood smear, and topological obstacles stemming from ambient contaminants present on the RBC surface are the main factors that could limit the capability of an AFM to resolve nanometer-sized protein aggregates on RBCs under standard laboratory conditions.

In the present work, we demonstrate that a thin air-dried blood smear sample (prepared by depositing ~50 μl of blood from memory clinic patients and healthy donors on glass slides), is well suited for conducting stable AFM measurements. The size, shape, morphology, assembly patterns, and prevalence of protein aggregates, which we term as physical biomarkers on RBCs from all patients, were quantified through analysis of height and phase-contrast AFM data. In general, the size of protein aggregates ranging from spherical/annular oligomers, protofibrils, to fibrils was observed to depend on the age of the patient, and the prevalence of fibrils increased with the severity of neurocognitive disorder of the patient. Furthermore, we present the correlative analysis of quantitative AFM measurements of fibrillar aggregates with the Aβ42/40 ratio in CSF, which might represent a promising screening biomarker of AD pathology.

RESULTS

For the RBC analysis, we recruited 50 patients from the memory clinic presenting cognitive complaints (26 female and 24 male subjects, of whom only 33 underwent a lumbar puncture). In addition, we examined identically prepared RBCs from 16 healthy donors using AFM as controls (see section S1 and figs. S1 and S2). Details on the diagnostic classification are provided in Materials and Methods. First, we present detailed AFM results based on surface analysis of RBCs from four patients (patient identification labels: KSSG-15: male, 53 years; KSSG-11: female, 69 years; KSSG-18: male, 76 years; and KSSG-38: male, 89 years). All four patients were clinically diagnosed to suffer from AD with evidence from the pathophysiological process (*39*), were amyloid positive as determined by an Aβ42/40 ratio < 0.068, and were classified as A+T+N+ (A, amyloid, T, tau, and N, neurodegeneration) according to the National Institute on Aging and Alzheimer's Association (NIA-AA) research framework (*8*). See table S1 for a summary of the clinical evaluation results for patients KSSG-11, 15, 18, and 38. The rationale for providing detailed surface analysis of RBCs specifically for these four patients with biomarker evidence of AD is to highlight that differences in morphology and assembly patterns of the protein aggregates can exist even when the patients only differ in age. Moreover, the protein aggregate morphology observed in these four abovementioned patients was also, to a large extent, representative of other patients who had a positive CSF Aβ42/40 ratio. The age, gender, and clinical diagnostic results of the patients were not revealed during AFM measurements and were only known to the clinicians involved in the study to avoid information bias during imaging experiments. The full spectrum of quantitative data on RBC surface analysis for all 50 patients is provided and correlated with the patient-specific clinical evaluation results.

Figure 1A is a three-dimensionally (3D) rendered AFM height image of a single RBC resolved within the blood smear sample (see

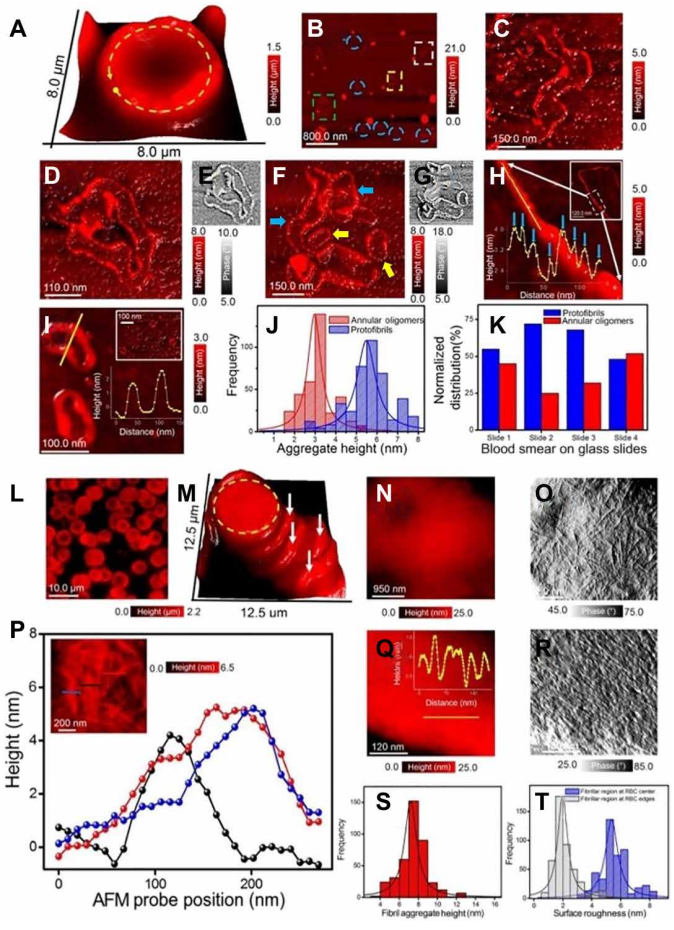

Fig. 1. Characterization of protein aggregates on RBCs from patients with AD. (**A**) 3D AFM image of RBC from a male patient aged 53 years with A+T+N+ classification. (**B**) AFM image at an RBC edge [indicated by the yellow circle in (A)]. (**C**) AFM image of protofibrils recorded in the region indicated by the dashed yellow box in (B). (**D** to **G**) Height and phase-contrast AFM images of protofibrils resolved at the region indicated by the white box in (B). The annular and irregularly shaped protofibrils are indicated by yellow and blue arrows in (F). (**H**) AFM image and sectional profile (shown in inset) of protofibril. (**I**) AFM height map and profile (shown in the bottom inset) of annular protofibrils. The top inset in (I) is an AFM image of annular oligomers detected within the blue circled region in the AFM image shown in (B). (**J**) The statistical plot provides a mean annular oligomer height (red histogram with Lorentzian fit) of 2.9 ± 0.7 nm and a mean protofibril height (blue histogram with Lorentzian fit) of 5.4 ± 1.1 nm. (**K**) Normalized distribution of annular oligomers and protofibrils detected on RBCs on four blood smear samples from the same patient. (**L**) Large-area and 3D AFM image (**M**) of RBCs from a female patient aged 69 years with A+T+N+ classification. (**N** and **O**) Height and phase-contrast image measured at the center of the RBC surface indicated by the yellow circle in (M). (**P**) Height traces measured across the fibrils marked by red, black, and blue lines in the AFM image shown in the top left inset of (P). (**Q** and **R**) Height and phase-contrast AFM images of dense fibrils recorded at RBC edges [marked with white arrows in (M)]. (**S**) Statistical plot provides a mean fibril height of 7.1 ± 1.5 nm. Surface roughness was measured at the RBC center (blue plot) and the RBC edges (gray plot). The gray and blue lines in the surface roughness plot (**T**) are a Lorentzian fit to the statistical data.

Materials and Methods for details on sample preparation and AFM details) prepared using blood drawn from a 53-year-old male patient (identified as patient number KSSG-15). The variations in height across the single RBCs are visible from the AFM topograph

shown in Fig. 1A (for large-area AFM images obtained on blood smear from patient KSSG-15, see fig. S3 and section S2). No major differences were observed from the large-area AFM images in the shape (predominantly discocyte shaped), height (~0.9 μm), or diameter (~6.5 μm) values between RBCs from healthy controls (see figs. S1 and S2) and patients with neurocognitive disorders. Closer examination of the RBCs, especially at the periphery (indicated by the yellow dashed circle in Fig. 1A), revealed nanostructures of varying geometries present at the RBC edges as shown in a representative AFM image (Fig. 1B). Adsorbates marked by blue circles in Fig. 1B are annular in shape, and adsorbates indicated by green, white, and yellow boxes in the same AFM image are those with fibrillar morphology. Figure 1C is a spatially magnified AFM image recorded within the region indicated by the yellow box in Fig. 1B, showing elongated strands with a distinct nodular morphology characteristic of protofibrillar aggregates observed along the aggregation pathway of amyloidogenic proteins (*26*, *40*–*42*). Similar height maps (Fig. 1, D and F) and corresponding phase-contrast data (Fig. 1, E and G) recorded within the green and white boxes in Fig. 1B reveal the nodular morphology of the protofibrillar adsorbates. The adsorbates indicated by yellow arrows in Fig. 1F correspond to annular-shaped structures, and the irregularly shaped strands are indicated by the blue arrows in Fig. 1F. Measuring at the edges of other RBCs present within the same blood smear sample confirmed the presence of similar protofibrillar and annular-shaped structures. Figure 1H is a high-resolution AFM topograph recorded on a different RBC from the same blood smear sample that reveals the presence of an elongated protofibril. The measured height profile (bottom inset in Fig. 1H) along the protofibril strand highlights the height differences originating from the nodes. Upon spatially magnifying on the blue circled regions in Fig. 1B, more annular oligomeric type aggregates (top inset in Fig. 1I) could be observed on the surface of the RBCs. On the basis of sectional profile analysis of all such adsorbates detected using the AFM, we calculate a mean height of 2.9 ± 0.7 nm for the annular oligomers (Fig. 1J, red histogram) and 5.4 ± 1.1 nm for the protofibrils (Fig. 1J, blue histogram). The statistical analysis of protofibril height includes measurements on both the irregularly shaped annular protofibrils and linearly shaped protofibrils. The normalized distribution of the annular oligomers and protofibrils over an area of 500 μm^2 of RBCs measured on four different blood smear samples is shown in Fig. 1K. On the basis of AFM measurements, we can confirm that these two specific types of protein aggregates were prevalent but not homogeneously distributed on the RBC surface. Instead, these aggregates were present mostly at the edges of the RBC. The protofibrillar aggregates resolved on the membrane of RBCs in our study are comparable in shape and size values to previous reports of tau (*31*, *43*), Aβ40 (*26*, *44*), and Aβ42 (*26*, *44*) protofibrils characterized in vitro using AFM. Likewise, annular oligomeric intermediates have also been confirmed to occur during the oligomerization of Aβ42 (*26*) and Zn-chelated Aβ40 and Aβ42 isoforms, which were also identified to be cytotoxic (*45*). Yet, irregularly shaped protofibrils appearing as a linearly packed string of spherical particles as in Fig. 1 (B to F) have, to the best of our knowledge, only been observed previously using AFM for the K-18 C291R variant of tau (prepared in buffer solution and deposited on mica surface for AFM imaging) (*46*).

Next, we analyzed the surface of RBCs present within blood smears prepared from a 69-year-old female patient (identified as patient number KSSG-11). Figure 1L is a large-area AFM topograph of a submonolayer coverage with a typical discocyte RBC shape on a glass slide. Spatially magnifying within the blood smear samples shows RBCs to also exist in a stacked confirmation as shown in the 3D rendered AFM image (Fig. 1M). Positioning the AFM probe and imaging within the center of the RBC region, indicated by the yellow circle in Fig. 1M, revealed the presence of elongated fibrillar aggregates, which were slightly visible from the height image (Fig. 1N). Optimizing the amplitude set point for an improved phase contrast (Fig. 1O) confirmed the presence of fibrils. Closer inspection of individual fibrils using AFM (see fig. S6 in section S2) showed a plain fibril morphology without the nodular structures previously observed for protofibrils detected on RBCs from patient KSSG-15. This observation indicates fibrillar structures resolved on RBCs from patient KSSG-11, which are probably mature fibrils composed of intertwined protofibrillar strands. Figure 1P shows a sectional analysis performed along multiple lines across the surface of an RBC (as shown in the corresponding AFM image in the top left inset of Fig. 1P). Cross-sectional profiles show the height differences of the fibrils within the network. Two-dimensional networks with comparable mature fibril height profiles have been resolved in the past using AFM for Aβ40 (*26*, *27*), (Aβ42) (*47*), and lithostathine (*48*) (an inflammatory protein overexpressed in patients with AD) under physiological conditions on synthetic surfaces, which can influence fibril morphology (*47*, *49*) and aggregation kinetics (*50*). Overall, the fibrils resolved in the central regions of RBCs from patient KSSG-11 were predominantly arranged in a branched network. However, positioning the AFM tip at the edges of the RBCs from the same patient showed a different fibrillar assembly pattern. Figure 1Q is an AFM topograph recorded at the edge site of an RBC from patient KSSG-11 showing the presence of closely packed fibrils. Simultaneously obtained phase-contrast data (Fig. 1R) from the same region as shown in Fig. 1Q provides rich details on the fibrillar assembly at the RBC edge. The fibril height of 7.1 ± 1.5 nm was determined from sectional profile analyses of individually resolved fibrils arranged in a branched network as shown in Fig. 1S (red histogram). In addition to the information on fibril height, the markedly different mean surface roughness of fibrils present at the center (blue histogram in Fig. 1T) and at the edges (gray histogram in Fig. 1T) of the RBCs from patient KSSG-11 was calculated to be 5.3 ± 1.1 nm and 1.9 ± 0.8 nm, respectively. Qualitative and quantitative information obtained from the AFM studies conducted thus far on A+T+N+ classified patients with AD aged 53 and 69 years clearly highlighted the variations in spatial organization and the differences in morphological profile of protein aggregates adsorbed on their respective RBCs.

Following the analysis of RBCs from patients with AD aged 53 and 69 years, we examined the RBCs from a 76-year-old male patient with AD (identified as patient number KSSG-18). Figure 2A is a large-area AFM image of well-resolved RBCs closely spaced within a blood smear on a glass slide. Following our regular imaging protocols, the AFM probe was first positioned within the center of the RBC indicated by the blue box in the large-area AFM image (Fig. 2A). Zooming in with the AFM probe at the marked region did not show any protuberant surface features (Fig. 2B). However, spatially magnifying further within the yellow box indicated in Fig. 2B revealed densely packed spherical particles (Fig. 2C), which are more discernable in the phase-contrast data (Fig. 2D). Cross-sectional analysis performed along the lines indicated in the AFM image

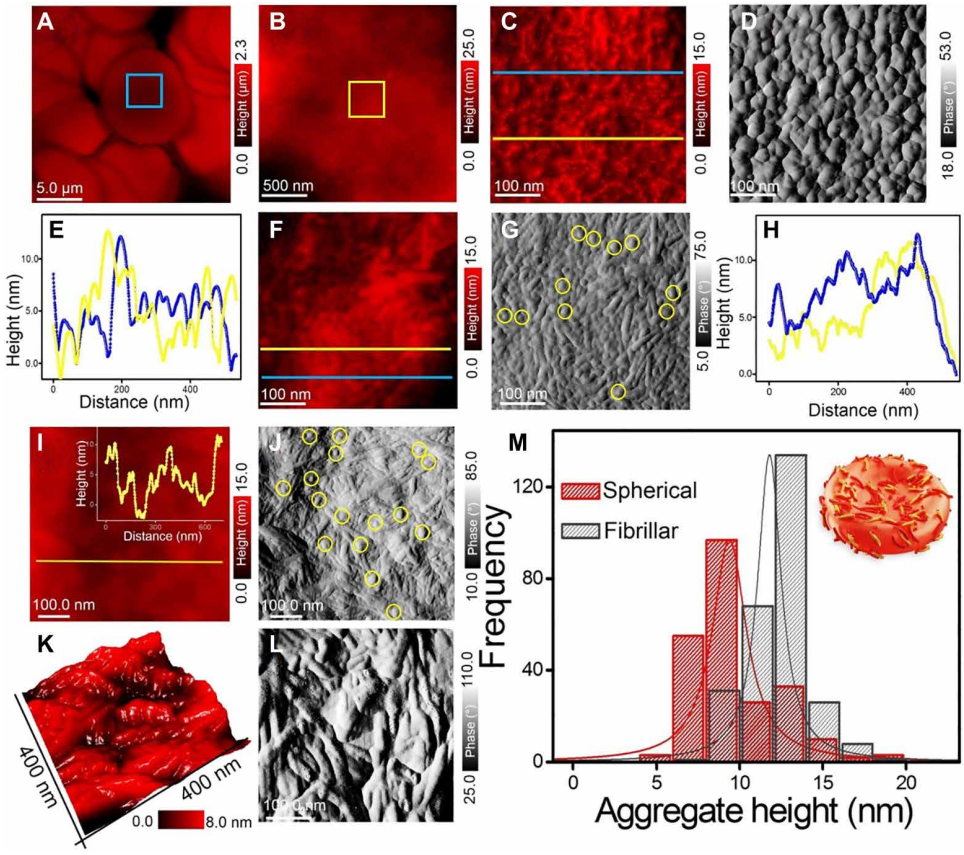

Fig. 2. Detection of spherical oligomeric and mature fibrillar aggregates on RBCs. (**A**) Large-area AFM image showing RBCs within the blood smear prepared from a male patient aged 76 years with A+T+N+ classification. (**B**) Zoomed-in AFM image recorded within the blue box marked in (A). (**C**) Spatially magnified AFM image obtained in the region marked by the yellow box in (B) showing a dense region of aggregates on the surface of the RBC. The almost spherical shape of the aggregates is better resolved in the simultaneously obtained phase-contrast AFM image (**D**). (**E**) Individual height profiles extracted along the blue and yellow lines indicated in (C) across spherical aggregates. (**F** and **G**) Height and the corresponding phase-contrast image recorded on a different RBC surface within the same blood smear sample showing the presence of predominantly fibrillar aggregates with intercalated spherical particles (marked by yellow circles). (**H**) Individual height profiles extracted along the blue and yellow lines indicated in (F) across a mixed population of fibrillar and spherical aggregates. (**I** and **J**) AFM height and phase-contrast image obtained on a different RBC surface within the blood smear samples prepared from blood drawn from patient KSSG-18 showing again the presence of fibrillar aggregates and a small population of spherical particles (indicted by yellow circles). The top left inset in (I) is the single height profile plot measured along the yellow line indicated in the AFM image (I). (**K**) High-resolution AFM image represented in 3D and the corresponding phase-contrast map (L) highlights the assembly of the fibrils on the RBC surface from the same patient. (**M**) The statistical plot of mean spherical aggregate height (red histogram) and mean fibrillar aggregate height distribution (gray histogram). The red and black lines in (M) are a Lorentzian fit to the spherical and fibrillar aggregate height histograms.

(Fig. 2B) is shown in Fig. 2E and highlights the local height differences of the spherical particles. Repositioning the AFM probe on a different RBC within the same blood smear sample revealed the presence of fibrillar aggregates (AFM height map, Fig. 2F) adsorbed with smaller spherical particles (indicated by the yellow circles in the phase-contrast data, Fig. 2G). Individual height profiles measured along the lines indicated in the AFM image (Fig. 2F) are shown in the height versus distance plot in Fig. 2H. Profiling similar topological information based on the height (Fig. 2I) and phase contrast (Fig. 2J) on another RBC within the same blood smear sample confirmed the coexistence of fibrillar and spherical aggregates (marked by yellow circles in Fig. 2J), which are adsorbed on the RBC surface. Figure 2K is a 3D-represented AFM image recorded on the fibrillar network (within the topographic region shown in Fig. 2I) revealing the dense fibrillar mesh, depicted more clearly in simultaneously recorded phase-contrast data (Fig. 2L). The optimization of phase-contrast images was an important step in our AFM measurements, allowing extraction of useful information that was often not immediately visible from height images. A clear result from the surface analysis of RBCs from patient KSSG-18 is the prevalent presence of fibrillar and spherical aggregates. The fibrillar and spherical aggregates were almost uniformly distributed across the RBC surface with no major difference in assembly patterns at RBC edges as previously observed in patients KSSG-15 and 11. In particular, fibrillar aggregates were observed to be more prevalent when compared to the spherical aggregates (see fig. S7 for details on the normalized distribution of fibrillar and spherical aggregates detected on the surface of RBCs from patient KSSG-18). On the basis of the height profile traces (similar to the plots shown in Fig. 2, E and H, and Fig. 2I, inset) measured on regions composed of both fibrillar and spherical aggregates, we extract a mean aggregate size of 9.3 ± 2.4 nm for the spherical particles (Fig. 2M, red histogram) and 11.8 ± 1.7 nm for fibrillar aggregates (Fig. 2M, gray histogram). Previously, the coexistence of mature fibrillar and spherically shaped

oligomeric aggregates has been reported and quantified using AFM for Aβ42 isoforms (*26*, *32*).

The surface analysis of RBCs from patients with AD aged 80 years and above revealed a markedly different topology when compared to younger patients who were amyloid positive and healthy controls. In this regard, we present results from surface analysis of RBCs from an 89-year-old male patient (identified as patient number KSSG-38), who is the oldest subject enrolled in the current study. Large-area AFM images (Fig. 3A) acquired within the blood smear sample revealed a marked difference in RBC surface characteristics compared to RBCs from healthy donors and previously analyzed patients with AD. The height (Fig. 3A) and phase-contrast (Fig. 3B) AFM data revealed a highly corrugated surface texture. On the basis of AFM image analysis of several hundreds of RBCs present within the blood smear sample from patient KSSG-38, we calculated a mean surface roughness of 48 ± 18 nm. The root mean square surface roughness value was normalized over an RBC area of 5 μm^2. The AFM measurements were conducted on the same day when the blood smears were prepared to avoid ambient contamination. The measured RBC surface roughness values for patient KSSG 38 is notably higher compared to the surface roughness of RBCs from healthy blood donors, which ranged from ~1.0 to 5.0 nm (see

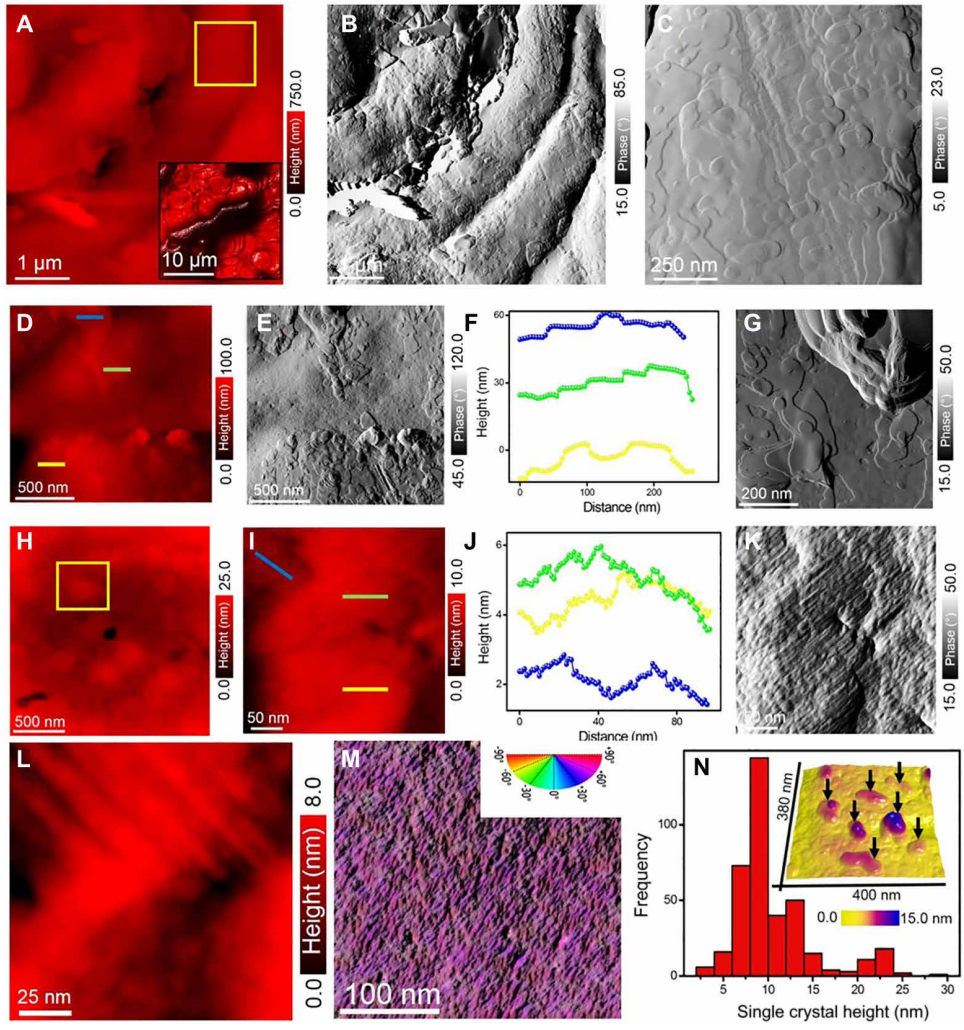

Fig. 3. Morphological evidence of protein crystals on RBCs from elderly patients with AD. AFM height (**A**) and phase-contrast image (**B**) showing a highly corrugated surface of RBCs from an 89-year-old male patient with A+T+N+ classification. Inset in (A) is a large-area 3D AFM height image of the closely packed RBCs. (**C**) Phase-contrast image recorded within the yellow box indicated in (A). The presence of domains on the RBC surface is visible from the phase-contrast images. (**D** and **E**) Height and simultaneously recorded phase-contrast image over another region on the same blood smear sample. The height profiles extracted along the blue, green, and yellow lines in (D) is plotted as individual sectional height traces in (**F**) showing the flat plateaus within the islands. (**G**) High-resolution phase-contrast AFM image showing the presence of domains that appear with varying height and morphology. (**H**) AFM images measured on a different location on the same sample reveals domains confirming the prevalent distribution of such features on RBCs within blood smears from the same patient. Spatially magnifying on a region within the domains reveals locally aligned fibrillar structures as observed from the height (**I**) and phase-contrast information (**K**) suggestive of crystallographic domains. (**J**) Height profile traces obtained along the blue, green, and yellow lines marked in the AFM height image (I). (**L**) AFM image showing individual aligned fibrils within crystal domains. (**M**) AFM phase-contrast image color-coded according to the fibril orientation angle. (**N**) Statistical plot of crystal domain size based on cross-sectional profile analysis extracted across individual crystals resolved in AFM images (see fig. S8). Inset in (N) is a 3D AFM image of individual and isolated protein crystals (indicated with black arrows) on the RBC surface showing height differences of the crystallographic domains.

figs. S1 and S2 in section S1 for details on surface roughness measurements on healthy controls).

A closer inspection of the surface topology revealed distinct domains present either as individual islands or in an overlapping and layered manner as shown in the phase-contrast image (Fig. 3C). Imaging at different locations on the same blood smear sample reveals a multitude of similar domains (Fig. 3, D and E) ranging in size from a few tens to hundreds of nanometers. The AFM height images indicate the domains to be of varying height profiles (Fig. 3F) and to be commonly distributed across the surface of the RBCs. The morphology of the domains is more clearly discernable from the phase-contrast images (Fig. 3, B, C, E, and G). Further examination of an individual domain (indicated in the yellow box in AFM image, Fig. 3H) through high-resolution AFM imaging revealed closely packed fibrillar aggregates as shown in the AFM height image (Fig. 3I) and the cross-sectional profiles (Fig. 3J). Figure 3K is a phase-contrast image highlighting the aligned fibrillar aggregates assembled within a domain, and a higher-resolution AFM image (Fig. 3L) shows the alignment at a single-fibril level. The observed alignment of the fibrils within smaller domains is shown in Fig. 3 (I and K) and was also detected within larger domains on the RBCs as shown in the phase-contrast AFM image (Fig. 3M), which was color-coded according to the fibril orientation angle. On the basis of the AFM observations, we attribute the domains composed of aligned and elongated fibrils to be protein crystals with a mean height of 9.9 ± 4.4 nm (Fig. 3N). Such protein crystals were only detected on RBCs from patients with AD aged 80 years and above within our study population (see fig. S8 in section S2 for further AFM measurements on additional protein crystals). Furthermore, the observation of mature and locally aligned fibrillar aggregates present in crystallographic domains on RBCs on only older patients with AD could also be an indication that protein crystals could be the ultimate end structures occurring along amyloid aggregation stages. This finding validates previous studies, which demonstrated that amyloid crystals (prepared under physiological buffered aqueous solution and resolved using AFM on synthetic solid surfaces) and not individual fibrillar aggregates occupy the ground state of protein folding energy landscape (*51*).

Following the in-depth description of the AFM results from the four exemplary patients, we present results from AFM-based analysis of RBCs for all 50 patients enrolled in the study. Figure 4 shows the distribution of mean protein aggregate size resolved using AFM on RBCs from all 50 patients plotted as a function of their age and grouped by the CSF amyloid status of the patients (see fig. S9 in section S2 for details on the plot of only mean fibrillar aggregate size as a function of patient age). The mean aggregate size data, shown in the plot, was obtained using the same AFM imaging protocols under identical experimental conditions when registering information on RBCs from patients KSSG-11, 15, 18, and 38 as shown in Figs. 1 to 3. An initial increase of aggregate size, associated with the patient age with a peak between 70 and 80 years, is observed from the scatterplot shown in Fig. 4. Thereafter, the mean aggregate size (for fibrils) tends to decrease again, which is also related to the more elongated and aligned features detected only for patients aged 80 and above. A similar trend in increased particle size as a function of declining cognition and memory function in patients has been reported previously using AFM in CSF medium (*38*). However, the AFM datasets in our study reveal clearer morphological profiles of the protein aggregates adsorbed on RBCs. For instance, fibrillar

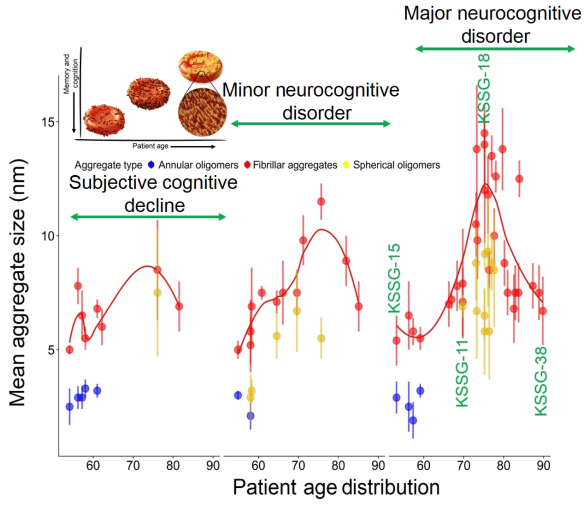

Fig. 4. Age dependence of protein aggregate morphology grouped by Aβ status. Scatterplot of the mean individual aggregate size of fibrillar aggregates and annular and spherical oligomers with ± 1 SD (based on AFM measurements on all 50 patients) plotted against the patient age and grouped by their amyloid status determined by the CSF Aβ42/40 ratio. Nonparametric, locally estimated scatterplot smoothing lines were added. A roughly bell-shaped nonlinear, nonmonotonic trend is observed where there is an overall increase in fibrillar protein aggregate size with increasing patient age up to a peak around the age of 70 to 80 and a subsequent decrease thereafter. The top left inset is a schematic summarizing our results on protein aggregate assembly on RBCs as a function of increasing patient age and decreasing cognition.

aggregates (data include both protofibrils and mature fibrils) were present in the blood smear samples of all age groups of patients (53 to 89 years). One unique finding during the AFM study was the aligned and elongated fibrillar aggregates present within crystallographic domains that were resolved only on RBCs of patients in the age group of 80 to 89 years, categorized as A+T+N+.

As the fibrils (including protofibrillar and elongated strands) were the only aggregate type present on RBCs of all 50 patients, we restricted our statistical analyses to the prevalence of fibrillar aggregate surface coverage. The plot showing the distribution (normalized over ~1000 RBCs) of fibrillar aggregates on RBCs of all patients and healthy elderly blood donors (age 45 to 68 years) across patient age and grouped by their associated neurocognitive syndrome highlights the importance of studying the prevalence of fibrillar aggregates (see fig. S10 in section S2). Additional results on the cognitive assessment test scores for all 50 patients are provided in fig. S11. The statistical analyses are focused only on the 33 patients in whom the CSF Aβ42/40 ratio was available. To be clear, a lumbar puncture was not mandatory for inclusion in the study, and the indication for the intervention was defined solely on clinical grounds. Especially in young patients without objective neuropsychological deficits as well as old patients with severe dementia, the benefit of determining the amyloid status must be balanced against the risks of the intervention. Furthermore, a portion of the patients did not consent to a lumbar puncture. In a multiple linear regression analysis, the CSF Aβ42/40 ratio was negatively correlated with the prevalence of fibrillar aggregates on RBC [t statistic (df = 29) = −2.61, P = 0.014]. In contrast, no significant correlation with CSF p-tau levels was found (P = 0.76), and we detected only a trend toward an increase in the prevalence of fibrillar aggregates with age (P = 0.059).

Full model results are presented in table S2. In a follow-up simple linear regression model, we confirmed a strong and highly significant negative correlation between the prevalence of fibrillar aggregates on RBC and the CSF Aβ42/40 ratio [$R = -0.64$, t statistic (31) = −4.69, $P < 0.001$; see Fig. 5A]. Post hoc t tests with Bonferroni corrections showed that the prevalence of fibrillar aggregates on RBC was significantly higher in the amyloid-positive group (mean: 69 ± 14% with $n = 18$) than in the amyloid-negative group [mean: 35 ± 21% with $n = 15$, t statistic (24) = −5.36, $P < 0.001$; see Fig. 5B]. The prevalence in the group with an undetermined amyloid status (mean: 55 ± 25% with $n = 17$) was also significantly higher than in the amyloid-negative group [t statistic (29.9) = −2.57, $P = 0.046$] and did not significantly differ from the amyloid-positive group ($P = 0.204$). Last, we evaluated whether the prevalence of fibrillar aggregates on RBC could accurately predict the amyloid status of patients determined by the CSF Aβ42/40 ratio as well as the CSF–p-tau status. The highest Youden index for classification of the amyloid status was found for a cutoff threshold of a fibrillary aggregate prevalence of ≥40%. Using this cutoff, all 18 amyloid-positive patients were identified [sensitivity and negative predictive value (npv) = 100%], whereas 4 patients were falsely classified as amyloid positive [specificity 74%, positive predictive value (ppv) = 81.8%], resulting in an overall classification accuracy of 88%. The receiver operating characteristic (ROC) curve and full diagnostic classification results are presented in Fig. 5C. The prevalence of fibrillary aggregates was also correlated with the p-tau status of patients with a prediction accuracy of 85% (see table S4 and fig. S12). The full clinical and diagnostic details of all the 50 patients enrolled in the study are provided in table S5.

DISCUSSION

In this study, we sought to investigate whether there are variations in physical features of aggregated forms of proteins on RBCs from patients with neurocognitive complaints. Using an AFM, we have successfully identified that differences exist in size, shape, morphology, assembly patterns, and prevalence of protein aggregates on RBCs from a clinically representative cohort of patients with memory and cognitive complaints. The morphological profile of protein aggregates, with shapes ranging from oligomers (spherical and annular-shaped), protofibrils (spherical particles arranged in a linear chain), and elongated fibrils (composed of twisted protofibrils), was studied on RBCs using AFM height maps and phase-contrast data. A general trend was observed from the AFM measurements for the prevalence of fibrillar protein aggregates to depend on the age and the level of decline in memory and cognition of the patients. In certain specific cases, there was evidence for coadsorption of spherical oligomeric particles and mature fibrils arranged in a densely packed network on the surface of RBCs for selected patients in the age group of 55 to

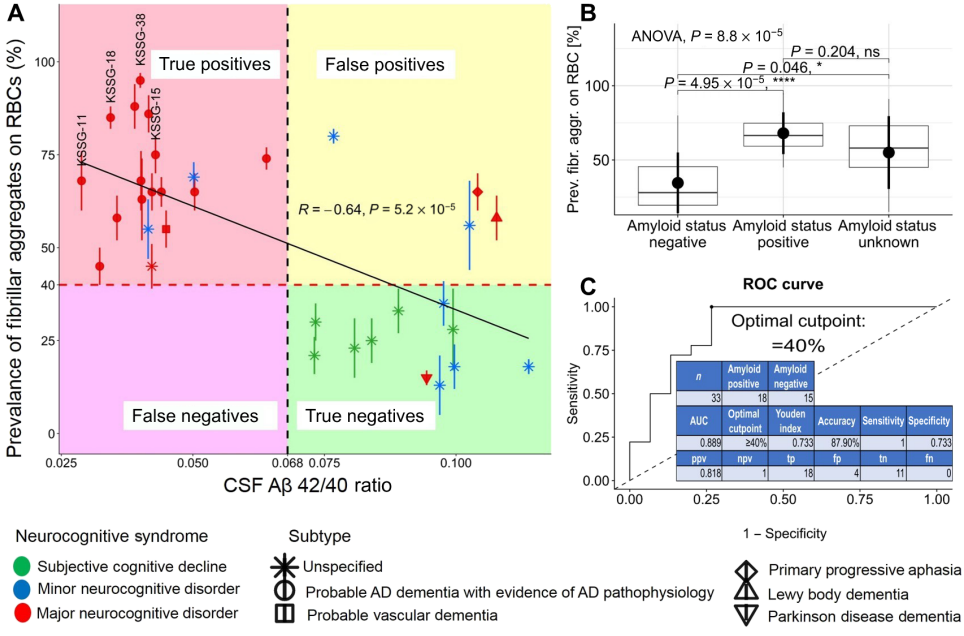

Fig. 5. Association of fibril prevalence on RBCs with the Aβ42/40 ratio in CSF and the performance as a diagnostic test. (**A**) Scatterplot of mean fibril prevalence (normalized over ~1000 RBCs) on RBC with ±1 SD plotted against the Aβ42/40 ratio in CSF of 33 patients who underwent a lumbar puncture showing a strong negative correlation. The neurocognitive syndromes were color-coded, and the individual etiologies/subtypes were shape-coded. When applying a prevalence cutoff of ≥40% (horizontal, dashed, red line), all 18 patients who were amyloid positive as determined by a CSF Aβ42/40 ratio < 0.068 (vertical, black, dashed line) were identified (sensitivity: 100%), whereas 4 patients were falsely classified as amyloid positive (specificity 74%), resulting in a classification accuracy of 88%. (**B**) Box-and-whiskers plots in the style of Tukey (central horizontal line: median, lower and upper hinges: 25th and 75th percentiles, upper and lower whiskers extend up 1.5 × interquartile ranges from the respective hinges) and the mean ± 1 SD of the prevalence of fibrils on RBCs grouped by the amyloid status of patients determined by the CSF Aβ42/40 ratio (no CSF available for amyloid status unknown group; $n = 17$). P values of a one-way ANOVA and t tests between groups with Bonferroni correction for multiple testing are presented, showing that fibril prevalence is lower in the amyloid-negative group than in both the amyloid-positive group and the group with unknown amyloid status. (**C**) Receiver operator characteristic (ROC) curve of a classification of the amyloid status (determined by the CSF-Aβ42/40 ratio) based on the prevalence of fibrillary aggregates on RBC and diagnostic performance measures (AUC, area under the curve; Youden index, sensitivity + specificity −1; ppv, positive predictive values; npv, negative predictive value; tp, true positives; fp, false positives; tn, true negatives; and fn, false negatives). ns, not significant.

78 years. Such oligomeric aggregates existing together with elongated fibrils have been discussed in the past to be potential targets for therapeutic intervention (*26*, *32*). Together, the AFM data reveal that nanoscopic differences in morphology and prevalence of protein aggregates on RBCs can be resolved and quantified in a label-free manner in blood smears.

One of the most notable findings that could be of immediate diagnostic relevance in our proof-of-principle study is the observation of aligned fibrillar deposits in the form of crystallographic domains on RBCs from patients aged 80 to 89 years who were clinically verified to be A+T+N+. If this result can be confirmed on a larger population of elderly patients with AD and validated with their CSF amyloid status, then in the future, this morphological signature could potentially be used as an additional physical biomarker of AD pathology. Furthermore, this information obtained from AFM can also be used as a first-line blood-based screening of elderly patients for AD pathology even within a clinical setting and also for monitoring the efficiency of prescribed treatment.

On the basis of the clinical evaluation results, AFM measurements on RBCs from both young and elderly healthy controls (see section S1) and in comparison with previous AFM-based studies on proteins involved in the pathology of AD (*26*, *27*, *29*–*31*, *37*, *46*, *52*), we postulate that the aggregates characterized on RBCs of all 50 patients here could mainly be a mixed composition of Aβ40, Aβ42, and tau protein isoforms. Although we demonstrated the morphological characterization of protein aggregates bound to RBCs, identification of the exact chemical signature of the resolved proteins is currently not feasible through only AFM-based measurements; hence, we cannot exclude the possible presence of other proteins implicated in the pathology of AD on RBCs from studied patients. The prevalence of fibrils that were present on RBCs of all 50 patients showed a strong negative correlation with the CSF Aβ42/40 ratio even when controlling for CSF–p-tau and patient age (Fig. 5A). Moreover, we found significant differences between the amyloid-positive and -negative patient groups (Fig. 5B). The evaluation of classifiers based on the prevalence of fibrillar aggregates on RBC yielded a high classification accuracy (88%) with high sensitivity and acceptable specificity when predicting the CSF amyloid status and good accuracy (85%) when predicting the CSF p-tau status. However, as the fibril prevalence was only correlated with the CSF Aβ42/40 but not the CSF p-tau levels in multiple regression analyses, the presented data suggest that these fibrillar aggregates may be strongly associated with the pathological accumulation of Aβ deposits in the brains of patients with AD.

In summary, our findings provide useful initial insights into the clinical relevance of nanoscopic information obtained by profiling protein aggregates on RBCs from patients with memory complaints and cognitive deficits. In particular, the data on the difference in size, shape, assembly patterns, and prevalence of the protein aggregates have been identified to form the basis for a complementary set of blood-based physical biomarkers of AD pathology. The ability to monitor the aggregated states of proteins through nanoscale imaging in blood could provide a deeper understanding of the molecular pathogenesis of AD, and the approach could be used to monitor the transition of cognitively healthy individuals to a preclinical phase of AD by screening blood smears in a regular time interval.

Several challenges lay ahead before physical biomarkers can be integrated with clinical decision-making for AD diagnosis. A logical approach in going forward is to verify the findings reported in our preclinical study of 50 patients in future studies with a larger cohort. In addition to morphological data, it will also be beneficial to simultaneously register the chemical signature of the resolved protein aggregates. For this, we propose using an AFM integrated with Raman or infrared spectroscopy to resolve the spectral peaks of the amide I, II, and III bands, which are known to be sensitive to the protein backbone conformation and secondary structures (*53*–*56*). The information from the deconvolution profile of these amide bands can then be expected to provide more detailed insights into the α helix and β sheet secondary structure, which will be key to identify the Aβ40, Aβ42, and tau isoforms present on the RBC surface. Such integrated AFM microscopes are commercially available and have been previously demonstrated to simultaneously map the morphology and chemical composition of pathological proteins on both clean surfaces (*52*, *54*–*57*) and in complex environments, such as the CSF (*37*), the neuronal spine (*58*), and brain tissues (*59*, *60*). There are numerous advantages of using AFM in clinical research and practice, including reduced instrumental complexity, easy to operate with basic training, built-in user-friendly software for data analysis, and capability to resolve even a few nanometer-sized particles under standard laboratory conditions. Limitations exist, such as the time involved in data acquisition and interpretation using an AFM compared to readouts from biochemical assays. Currently, it takes 3 to 5 days to provide a complete AFM-based imaging of blood smear samples from a single patient and providing the analyzed data (qualitative and quantitative) in a digitized format that can be understood by non-AFM experts. Although this period is an issue for screening rapidly progressing diseases, given the slow-progressing nature of AD and the time it takes (order of several weeks) to reach clinical consensus based on CSF biomarkers, brain imaging, and cognitive assessment, it should be possible to integrate the physical biomarker data upon validation with existing standards into the clinical decision-making pipeline. At the outset, we anticipate that the affordable and accessible physical biomarkers could serve as complementary metrics for screening patients with AD in the preclinical, mildly cognitively affected stages of AD, and possibly even prodromal, i.e., asymptomatic, stages of AD pathology.

MATERIALS AND METHODS

Patient characteristics

Here, we present data from the first 50 patients recruited as part of an ongoing study who presented themselves for an initial or follow-up assessment of cognitive complaints at the memory clinic of the Department of Neurology at the Cantonal Hospital St. Gallen. A lumbar puncture was performed in 39 patients. However, in two of these patients, the lumbar puncture was performed >1 month before the inclusion in the study, and Aβ40 was not determined. Moreover, in four patients, CSF analyses yielded implausible measures (both Aβ42 and Aβ40 decreased) pointing toward a preanalytical or analytical error. Consequently, the amyloid status as assessed by the CSF Aβ42/40 ratio (positive: <0.068) could only be reliably assessed in 33 cases. The severity of cognitive impairments and the clinical diagnosis of the patients were heterogeneous. We classified the severity of neurocognitive disorder according to the Diagnostic and Statistical Manual of Mental Disorders syndrome classification of neurocognitive disorders (*61*) as minor or major neurocognitive disorder or as subjective cognitive disorder according to (*62*) if criteria for the former were not fulfilled. Eight patients were diagnosed with subjective cognitive

decline, 12 patients with minor neurocognitive disorder, and 30 patients with major neurocognitive disorder. No patient with subjective decline had a positive CSF Aβ42/40 ratio. In contrast, the CSF Aβ42/40 ratio was decreased in 2 patients with minor neurocognitive disorder as well as in 16 of 30 patients with major neurocognitive disorder, which is indicative of the AD pathophysiological process (*63*). Fourteen of the latter and two additional patients with indicative atrophy pattern for whom the CSF was not obtained fulfilled the clinical NIA-AA criteria of probable AD dementia with evidence of the AD pathophysiological process (*39*). Furthermore, two dementia patients were diagnosed with clinically probable AD dementia without biomarker evidence of the AD pathophysiological process (*39*), three with primary progressive aphasia (*64*), two with probable vascular dementia (*65*), one with posterior cortical atrophy (*66*), one with Lewy body dementia, and one with Parkinson disease dementia (*67*). The dementia etiology could not be determined in two cases. The choice of neuropsychological tests was not affected by study participation. The Montreal Cognitive Assessment was administered in 42 patients and the Mini-Mental State Examination was administered in 5 patients. Summaries of the demographic, clinical evaluation, CSF analysis, and experimental data of the patients are grouped by the amyloid status as determined by the CSF Aβ42/40 ratio and are presented in table S2 with exploratory between-groups analysis of variance (ANOVA) or chi-square tests. To be eligible for inclusion in the study, the patient's routine diagnostic workup must have consisted of neuropsychological testing, routine blood tests, and structural magnetic resonance imaging of the brain. However, further routine diagnostic workup was not influenced by the inclusion in the study, and the indication for a lumbar puncture was exclusively defined on clinical grounds. All diagnoses were made in an interdisciplinary conference and reviewed following the respective diagnostic criteria. All participants gave informed consent to participate in the study. The experimental procedures were approved by the ethics committee of East Switzerland (number: 202000558) and were performed following the Declaration of Helsinki.

AFM setup, measurements, and analysis

AFM measurements on the air-dried blood smear samples (~50 μl of blood from each patient was prepared as a smear on a glass slide) were performed using Multimode 8 for high-resolution imaging (with e-scanner, Bruker) and Dimension Icon (Bruker) for large-area imaging. Both AFM instruments were operated under standard laboratory conditions. For measurements using Multimode 8, the glass slides were first cleaved with a diamond cutter to a size of ~1 cm^2, adhered to a circular metal disk using a double-sided sticky tape, and then mounted on top of the tube scanner followed by positioning the probe holder for imaging. For the AFM probe, a SCOUT 70 HAR silicon AFM tip with a high aspect ratio (gold reflective backside coating, force constant 2 N/m, resonant frequency: 70 kHz, cone angle of <15° over the final 1 μm of the tip apex; NuNano) was used in tapping mode. All AFM measurements were conducted at a scan rate of 0.5 to 1 Hz. Upon receiving the AFM tips in a gel pack from NuNano, the tips were transferred to a normal plastic tip holder to avoid tip contamination by the gel pack. Before placing the AFM tip in the holder, it was cleaned by rinsing in acetone for 30 s followed by rinsing in isopropanol for ~1 min and by blow-drying with compressed air. The values for the SD reported for the height of the protein aggregates were calculated from measurements performed with five AFM tips from the same batch purchased from NuNano. All AFM measurements on the blood smear samples were performed within 10 to 24 hours from the preparation of the blood smears on the glass slides. After initial surface analysis, the selected samples (blood smears samples that required more detailed investigation) were coated with silicone oil to prevent ambient contamination. For AFM measurements on silicone liquid-coated blood smear samples, identical materials (silicone oil purchased from Sigma-Aldrich, 317677), deposition technique (spray deposition using Harder and Steenbeck dual-action evolution spray gun), and imaging parameters as previously reported by Nirmalraj *et al.* (*68*) for resolving fixed and dried epithelial cells were adopted here. For image processing, the raw AFM data were analyzed using Nanoscope analysis 1.9 (Bruker) and subjected to first-order flattening before extraction of height profile and surface roughness values from the topographic information. The orientation map of aligned fibrils shown in Fig. 3M was analyzed using Fiberapp, open-source software (*69*). For AFM measurements on blood smears from healthy controls and patients enrolled in the study, a total of nearly 1000 RBCs were analyzed for each case. In general, ~50 to 80 RBCs could be resolved within a 60-μm^2 scan area, and ~30 to 50 of such large area images were required to be recorded at different locations on the glass slide to develop a comprehensive overview of the RBC surface topology. Ideally, RBCs that were isolated within the blood smear were well suited for profiling their surface using an ultrasharp AFM probe.

Statistical analyses regarding the prevalence of fibrillar aggregates on RBC

We performed multiple linear regression analysis of the dependent variable prevalence of fibrillar aggregates on RBCs with the following predictors: CSF Aβ42/40 ratio, CSF–p-tau, and patient age. All predictor variables were centered on the population mean. This was followed up by pairwise *t* tests with Bonferroni correction between patients with positive (CSF Aβ42/40 ratio < 0.068), negative (CSF Aβ42/40 ratio ≥ 0.068), and unknown (no lumbar puncture performed) amyloid status. Furthermore, we conducted exploratory simple linear regression between the CSF Aβ42/40 ratio and the prevalence of fibrillar aggregates on RBCs. We determined the threshold of the prevalence of fibrillar aggregates on RBCs to differentiate between amyloid-positive and -negative patients according to the CSF Aβ42/40 ratio that yielded the highest Youden index (sensitivity + specificity −1). An ROC curve and classification performance measure area under the curve, accuracy, sensitivity, specificity, Youden index, ppv, npv, true positives, false positives, true negatives, and false negatives. In an exploratory additional analysis, we evaluated the classification performance of the CSF–p-tau status based on the prevalence of fibrillar aggregates on RBCs. Performance measures were calculated for (i) a cutoff yielding the highest Youden index (≥50%) and (ii) a cutoff yielding the highest product of the ppvs and npvs (≥ 40%).

SUPPLEMENTARY MATERIALS

Supplementary material for this article is available at https://science.org/doi/10.1126/sciadv.abj2137

View/request a protocol for this paper from *Bio-protocol*.

REFERENCES AND NOTES

1. J. D. Doecke, V. Pérez-Grijalba, N. Fandos, C. Fowler, V. L. Villemagne, C. L. Masters, P. Pesini, M. Sarasa; for the AIBL Research Group, Total Aβ42/Aβ40 ratio in plasma predicts amyloid-PET status, independent of clinical AD diagnosis. *Neurology* **94**, e1580–e1591 (2020).

2. 2020 Alzheimer's disease facts and figures. *Alzheimers Dement.* **16**, 391–460 (2020).
3. B. T. Hyman, C. H. Phelps, T. G. Beach, E. H. Bigio, N. J. Cairns, M. C. Carrillo, D. W. Dickson, C. Duyckaerts, M. P. Frosch, E. Masliah, S. S. Mirra, P. T. Nelson, J. A. Schneider, D. R. Thal, B. Thies, J. Q. Trojanowski, H. V. Vinters, T. J. Montine, National Institute on Aging-Alzheimer's Association guidelines for the neuropathologic assessment of Alzheimer's disease. *Alzheimers Dement.* **8**, 1–13 (2012).
4. C. L. Masters, R. Bateman, K. Blennow, C. C. Rowe, R. A. Sperling, J. L. Cummings, Alzheimer's disease. *Nat. Rev. Dis. Primers.* **1**, 15056 (2015).
5. P. E. Spies, D. Slats, J. M. C. Sjögren, B. P. H. Kremer, F. R. J. Verhey, M. G. M. Olde Rikkert, M. M. Verbeek, The cerebrospinal fluid amyloid β42/40 ratio in the differentiation of Alzheimer's disease from non-Alzheimer's dementia. *Curr. Alzheimer Res.* **7**, 470–476 (2010).
6. S. M. Landau, B. A. Thomas, L. Thurfjell, M. Schmidt, R. Margolin, M. Mintun, M. Pontecorvo, S. L. Baker, W. J. Jagust; Alzheimer's Disease Neuroimaging Initiative, Amyloid PET imaging in Alzheimer's disease: A comparison of three radiotracers. *Eur. J. Nucl. Med. Mol. Imaging* **41**, 1398–1407 (2014).
7. N. Mattsson, M. C. Carrillo, R. A. Dean, M. D. Devous Sr., T. Nikolcheva, P. Pesini, H. Salter, W. Z. Potter, R. S. Sperling, R. J. Bateman, L. J. Bain, E. Liu, Revolutionizing Alzheimer's disease and clinical trials through biomarkers. *Alzheimers Dement* **1**, 412–419 (2015).
8. C. R. Jack Jr., D. A. Bennett, K. Blennow, M. C. Carrillo, B. Dunn, S. B. Haeberlein, D. M. Holtzman, W. Jagust, F. Jessen, J. Karlawish, E. Liu, J. L. Molinuevo, T. Montine, C. Phelps, K. P. Rankin, C. C. Rowe, P. Scheltens, E. Siemers, H. M. Snyder, R. Sperling, C. Elliott, E. Masliah, L. Ryan, N. Silverberg, NIA-AA research framework: Toward a biological definition of Alzheimer's disease. *Alzheimers Dement.* **14**, 535–562 (2018).
9. A. Vergallo, L. Mégret, S. Lista, E. Cavedo, H. Zetterberg, K. Blennow, E. Vanmechelen, A. de Vos, M. O. Habert, M. C. Potier, B. Dubois, C. Neri, H. Hampel; and the INSIGHT-preAD study group; for the Alzheimer Precision Medicine Initiative (APMI), Plasma amyloid β 40/42 ratio predicts cerebral amyloidosis in cognitively normal individuals at risk for Alzheimer's disease. *Alzheimers Dement.* **15**, 764–775 (2019).
10. S. E. Schindler, J. G. Bollinger, V. Ovod, K. G. Mawuenyega, Y. Li, B. A. Gordon, D. M. Holtzman, J. C. Morris, T. L. S. Benzinger, C. Xiong, A. M. Fagan, R. J. Bateman, High-precision plasma β-amyloid 42/40 predicts current and future brain amyloidosis. *Neurology* **93**, e1647–e1659 (2019).
11. T. K. Karikari, T. A. Pascoal, N. J. Ashton, S. Janelidze, A. L. Benedet, J. L. Rodriguez, M. Chamoun, M. Savard, M. S. Kang, J. Therriault, M. Schöll, G. Massarweh, J. P. Soucy, K. Höglund, G. Brinkmalm, N. Mattsson, S. Palmqvist, S. Gauthier, E. Stomrud, H. Zetterberg, O. Hansson, P. Rosa-Neto, K. Blennow, Blood phosphorylated tau 181 as a biomarker for Alzheimer's disease: A diagnostic performance and prediction modelling study using data from four prospective cohorts. *Lancet Neurol.* **19**, 422–433 (2020).
12. S. Palmqvist, S. Janelidze, Y. T. Quiroz, H. Zetterberg, F. Lopera, E. Stomrud, Y. Su, Y. Chen, G. E. Serrano, A. Leuzy, N. Mattsson-Carlgren, O. Strandberg, R. Smith, A. Villegas, D. Sepulveda-Falla, X. Chai, N. K. Proctor, T. G. Beach, K. Blennow, J. L. Dage, E. M. Reiman, O. Hansson, Discriminative accuracy of plasma phospho-tau217 for Alzheimer disease vs other neurodegenerative disorders. *JAMA* **324**, 772–781 (2020).
13. N. Fandos, V. Pérez-Grijalba, P. Pesini, S. Olmos, M. Bossa, V. L. Villemagne, J. Doecke, C. Fowler, C. L. Masters, M. Sarasa; AIBL Research Group, Plasma amyloid β 42/40 ratios as biomarkers for amyloid β cerebral deposition in cognitively normal individuals. *Alzheimers Dement.* **8**, 179–187 (2017).
14. N. C. Cullen, A. Leuzy, S. Palmqvist, S. Janelidze, E. Stomrud, P. Pesini, L. Sarasa, J. A. Allué, N. K. Proctor, H. Zetterberg, J. L. Dage, K. Blennow, N. Mattsson-Carlgren, O. Hansson, Individualized prognosis of cognitive decline and dementia in mild cognitive impairment based on plasma biomarker combinations. *Nat. Aging* **1**, 114–123 (2021).
15. J. C. Lee, S. J. Kim, S. Hong, Y. Kim, Diagnosis of Alzheimer's disease utilizing amyloid and tau as fluid biomarkers. *Exp. Mol. Med.* **51**, 1–10 (2019).
16. P. S. Aisen, J. Cummings, C. R. Jack Jr., J. C. Morris, R. Sperling, L. Frölich, R. W. Jones, S. A. Dowsett, B. R. Matthews, J. Raskin, P. Scheltens, B. Dubois, On the path to 2025: Understanding the Alzheimer's disease continuum. *Alzheimers Res. Ther.* **9**, 60 (2017).
17. A. Nabers, L. Perna, J. Lange, U. Mons, J. Schartner, J. Güldenhaupt, K. U. Saum, S. Janelidze, B. Holleczek, D. Rujescu, O. Hansson, K. Gerwert, H. Brenner, Amyloid blood biomarker detects Alzheimer's disease. *EMBO Mol. Med.* **10**, e8763 (2018).
18. Y. K. Yoo, J. Kim, G. Kim, Y. S. Kim, H. Y. Kim, S. Lee, W. W. Cho, S. Kim, S. M. Lee, B. C. Lee, J. H. Lee, K. S. Hwang, A highly sensitive plasma-based amyloid-β detection system through medium-changing and noise cancellation system for early diagnosis of the Alzheimer's disease. *Sci. Rep.* **7**, 8882 (2017).
19. A. Nakamura, N. Kaneko, V. L. Villemagne, T. Kato, J. Doecke, V. Doré, C. Fowler, Q.-X. Li, R. Martins, C. Rowe, T. Tomita, K. Matsuzaki, K. Ishii, K. Ishii, Y. Arahata, S. Iwamoto, K. Ito, K. Tanaka, C. L. Masters, K. Yanagisawa, High performance plasma amyloid-β biomarkers for Alzheimer's disease. *Nature* **554**, 249–254 (2018).
20. J. Lan, J. Liu, Z. Zhao, R. Xue, N. Zhang, P. Zhang, P. Zhao, F. Zheng, X. Sun, The peripheral blood of Aβ binding RBC as a biomarker for diagnosis of Alzheimer's disease. *Age Ageing* **44**, 458–464 (2015).
21. S. Daniele, D. Pietrobono, J. Fusi, C. Iofrida, L. Chico, L. Petrozzi, A. L. Gerfo, F. Baldacci, F. Galetta, G. Siciliano, U. Bonuccelli, G. Santoro, M. L. Trincavelli, F. Franzoni, C. Martini, α-Synuclein aggregates with β-amyloid or Tau in human red blood cells: Correlation with antioxidant capability and physical exercise in human healthy subjects. *Mol. Neurobiol.* **55**, 2653–2675 (2018).
22. W. A. Banks, A. Kovac, P. Majerova, K. M. Bullock, M. Shi, J. Zhang, Tau proteins cross the blood-brain barrier. *J. Alzheimers Dis.* **55**, 411–419 (2017).
23. E. Zenaro, G. Piacentino, G. Constantin, The blood-brain barrier in Alzheimer's disease. *Neurobiol. Dis.* **107**, 41–56 (2017).
24. X. Deng, F. Xiong, X. Li, B. Xiang, Z. Li, X. Wu, C. Guo, X. Li, Y. Li, G. Li, W. Xiong, Z. Zeng, Application of atomic force microscopy in cancer research. *J. Nanobiotechnol.* **16**, 102 (2018).
25. M. Stolz, R. Gottardi, R. Raiteri, S. Miot, I. Martin, R. Imer, U. Staufer, A. Raducanu, M. Düggelin, W. Baschong, A. U. Daniels, N. F. Friederich, A. Aszodi, U. Aebi, Early detection of aging cartilage and osteoarthritis in mice and patient samples using atomic force microscopy. *Nat. Nanotechnol.* **4**, 186–192 (2009).
26. P. N. Nirmalraj, J. List, S. Battacharya, G. Howe, L. Xu, D. Thompson, M. Mayer, Complete aggregation pathway of amyloid β (1-40) and (1-42) resolved on an atomically clean interface. *Sci. Adv.* **6**, eaaz6014 (2020).
27. Y.-C. Lin, H. Komatsu, J. Ma, P. H. Axelsen, Z. Fakhraai, Identifying polymorphs of amyloid-β (1–40) fibrils using high-resolution atomic force microscopy. *J. Phys. Chem. B.* **123**, 10376–10383 (2019).
28. T. Watanabe-Nakayama, K. Ono, M. Itami, R. Takahashi, D. B. Teplow, M. Yamada, High-speed atomic force microscopy reveals structural dynamics of amyloid β1-42 aggregates. *Proc. Natl. Acad. Sci. U.S.A.* **113**, 5835–5840 (2016).
29. S. Maity, Y. L. Lyubchenko, AFM probing of amyloid-β 42 dimers and trimers. *Front. Mol. Biosci.* **7**, (2020).
30. A. Barrantes, J. Sotres, M. Hernando-Pérez, M. J. Benítez, P. J. de Pablo, A. M. Baró, J. Ávila, J. S. Jiménez, Tau aggregation followed by atomic force microscopy and surface plasmon resonance, and single molecule tau-tau interaction probed by atomic force spectroscopy. *J. Alzheimers Dis.* **18**, 141–151 (2009).
31. S. Wegmann, I. D. Medalsy, E. Mandelkow, D. J. Müller, The fuzzy coat of pathological human Tau fibrils is a two-layered polyelectrolyte brush. *Proc. Natl. Acad. Sci.* **110**, E313 (2013).
32. C. Tinker-Mill, J. Mayes, D. Allsop, O. V. Kolosov, Ultrasonic force microscopy for nanomechanical characterization of early and late-stage amyloid-β peptide aggregation. *Sci. Rep.* **4**, 4004 (2014).
33. N. Yeow, R. F. Tabor, G. Garnier, Atomic force microscopy: From red blood cells to immunohaematology. *Adv. Colloid Interface Sci.* **249**, 149–162 (2017).
34. P. Zachée, J. Snauwaert, P. Vandenberghe, L. Hellemans, M. Boogaerts, Imaging red blood cells with the atomic force microscope. *Br. J. Haematol.* **95**, 472–481 (1996).
35. R. Nowakowski, P. Luckham, P. Winlove, Imaging erythrocytes under physiological conditions by atomic force microscopy. *Biochim. Biophys. Acta.* **1514**, 170–176 (2001).
36. M. S. AlSalhi, S. Devanesan, K. E. Al Zahrani, M. A. Shebly, F. Al-Qahtani, K. Farhat, V. Masilamani, Impact of diabetes mellitus on human erythrocytes: Atomic force microscopy and spectral investigations. *Int. J. Environ. Res. Public Health* **15**, 2368 (2018).
37. S. De, D. R. Whiten, F. S. Ruggeri, C. Hughes, M. Rodrigues, D. I. Sideris, C. G. Taylor, F. A. Aprile, S. Muyldermans, T. P. J. Knowles, M. Vendruscolo, C. Bryant, K. Blennow, I. Skoog, S. Kern, H. Zetterberg, D. Klenerman, Soluble aggregates present in cerebrospinal fluid change in size and mechanism of toxicity during Alzheimer's disease progression. *Acta Neuropathol. Commun.* **7**, 120 (2019).
38. T. Yue, X. Jia, J. Petrosino, L. Sun, Z. Fan, J. Fine, R. Davis, S. Galster, J. Kuret, D. W. Scharre, M. Zhang, Computational integration of nanoscale physical biomarkers and cognitive assessments for Alzheimer's disease diagnosis and prognosis. *Sci. Adv.* **3**, e1700669 (2017).
39. G. M. McKhann, D. S. Knopman, H. Chertkow, B. T. Hyman, C. R. Jack Jr., C. H. Kawas, W. E. Klunk, W. J. Koroshetz, J. J. Manly, R. Mayeux, R. C. Mohs, J. C. Morris, M. N. Rossor, P. Scheltens, M. C. Carrillo, B. Thies, S. Weintraub, C. H. Phelps, The diagnosis of dementia due to Alzheimer's disease: Recommendations from the National Institute on Aging-Alzheimer's Association workgroups on diagnostic guidelines for Alzheimer's disease. *Alzheimers Dement.* **7**, 263–269 (2011).
40. R. Kayed, A. Pensalfini, L. Margol, Y. Sokolov, F. Sarsoza, E. Head, J. Hall, C. Glabe, Annular protofibrils are a structurally and functionally distinct type of amyloid oligomer. *J. Biol. Chem.* **284**, 4230–4237 (2009).
41. I. A. Mastrangelo, M. Ahmed, T. Sato, W. Liu, C. Wang, P. Hough, S. O. Smith, High-resolution atomic force microscopy of soluble Aβ42 oligomers. *J. Mol. Biol.* **358**, 106–119 (2006).
42. J. D. Harper, S. S. Wong, C. M. Lieber, P. T. Lansbury, Observation of metastable Aβ amyloid protofibrils by atomic force microscopy. *Chem. Biol.* **4**, 119–125 (1997).
43. S. Xu, K. R. Brunden, J. Q. Trojanowski, V. M. Y. Lee, Characterization of tau fibrillization in vitro. *Alzheimers Dement.* **6**, 110–117 (2010).

44. J. D. Harper, S. S. Wong, C. M. Lieber, P. T. Lansbury, Observation of metastable Abeta amyloid protofibrils by atomic force microscopy. *Chem. Biol.* **4**, 119–125 (1997).
45. M.-C. Lee, W. C. Yu, Y. H. Shih, C. Y. Chen, Z. H. Guo, S. J. Huang, J. C. C. Chan, Y. R. Chen, Zinc ion rapidly induces toxic, off-pathway amyloid-β oligomers distinct from amyloid-β derived diffusible ligands in Alzheimer's disease. *Sci. Rep.* **8**, 4772 (2018).
46. T. K. Karikari, R. Thomas, K. G. Moffat, The C291R tau variant forms different types of protofibrils. *Front. Mol. Neurosci.* **13**, (2020).
47. B. Moores, E. Drolle, S. J. Attwood, J. Simons, Z. Leonenko, Effect of surfaces on amyloid fibril formation. *PLOS ONE* **6**, e25954 (2011).
48. P.-E. Milhiet, D. Yamamoto, O. Berthoumieu, P. Dosset, C. L. Grimellec, J.-M. Verdier, S. Marchal, T. Ando, Deciphering the structure, growth and assembly of amyloid-like fibrils using high-speed atomic force microscopy. *PLOS ONE* **5**, e13240 (2010).
49. Y.-C. Lin, E. J. Petersson, Z. Fakhraai, Surface effects mediate self-assembly of amyloid-β peptides. *ACS Nano* **8**, 10178–10186 (2014).
50. R. Vácha, S. Linse, M. Lund, Surface effects on aggregation kinetics of amyloidogenic peptides. *J. Am. Chem. Soc.* **136**, 11776–11782 (2014).
51. N. P. Reynolds, J. Adamcik, J. T. Berryman, S. Handschin, A. A. H. Zanjani, W. Li, K. Liu, A. Zhang, R. Mezzenga, Competition between crystal and fibril formation in molecular mutations of amyloidogenic peptides. *Nat. Commun.* **8**, 1338 (2017).
52. J. F. Smith, T. P. J. Knowles, C. M. Dobson, C. E. MacPhee, M. E. Welland, Characterization of the nanoscale properties of individual amyloid fibrils. *Proc. Natl. Acad. Sci.* **103**, 15806–15811 (2006).
53. F. S. Ruggeri, B. Mannini, R. Schmid, M. Vendruscolo, T. P. J. Knowles, Single molecule secondary structure determination of proteins through infrared absorption nanospectroscopy. *Nat. Commun.* **11**, 2945 (2020).
54. F. S. Ruggeri, J. Habchi, S. Chia, R. I. Horne, M. Vendruscolo, T. P. J. Knowles, Infrared nanospectroscopy reveals the molecular interaction fingerprint of an aggregation inhibitor with single Aβ42 oligomers. *Nat. Commun.* **12**, 688 (2021).
55. C. Blum, T. Schmid, L. Opilik, S. Weidmann, S. R. Fagerer, R. Zenobi, Understanding tip-enhanced Raman spectra of biological molecules: A combined Raman, SERS and TERS study. *J. Raman Spectrosc.* **43**, 1895–1904 (2012).
56. E. Lipiec, D. Perez-Guaita, J. Kaderli, B. R. Wood, R. Zenobi, Direct nanospectroscopic verification of the amyloid aggregation pathway. *Angew. Chem. Int. Ed.* **57**, 8519–8524 (2018).
57. F. S. Ruggeri, G. Longo, S. Faggiano, E. Lipiec, A. Pastore, G. Dietler, Infrared nanospectroscopy characterization of oligomeric and fibrillar aggregates during amyloid formation. *Nat. Commun.* **6**, 7831 (2015).
58. M. Tabatabaei, F. A. Caetano, F. Pashee, S. S. G. Ferguson, F. Lagugné-Labarthet, Tip-enhanced Raman spectroscopy of amyloid β at neuronal spines. *Analyst* **142**, 4415–4421 (2017).
59. B. Lochocki, T. H. J. Morrema, F. Ariese, J. J. M. Hoozemans, J. F. de Boer, The search for a unique Raman signature of amyloid-beta plaques in human brain tissue from Alzheimer's disease patients. *Analyst* **145**, 1724–1736 (2020).
60. M. Ji, M. Arbel, L. Zhang, C. W. Freudiger, S. S. Hou, D. Lin, X. Yang, B. J. Bacskai, X. S. Xie, Label-free imaging of amyloid plaques in Alzheimer's disease with stimulated Raman scattering microscopy. *Sci. Adv.* **4**, eaat7715 (2018).
61. P. S. Sachdev, D. Blacker, D. G. Blazer, M. Ganguli, D. V. Jeste, J. S. Paulsen, R. C. Petersen, Classifying neurocognitive disorders: The DSM-5 approach. *Nat. Rev. Neurol.* **10**, 634–642 (2014).
62. F. Jessen, R. E. Amariglio, M. van Boxtel, M. Breteler, M. Ceccaldi, G. Chételat, B. Dubois, C. Dufouil, K. A. Ellis, W. M. van der Flier, L. Glodzik, A. C. van Harten, M. J. de Leon, P. McHugh, M. M. Mielke, J. L. Molinuevo, L. Mosconi, R. S. Osorio, A. Perrotin, R. C. Petersen, L. A. Rabin, L. Rami, B. Reisberg, D. M. Rentz, P. S. Sachdev, V. de la Sayette, A. J. Saykin, P. Scheltens, M. B. Shulman, M. J. Slavin, R. A. Sperling, R. Stewart, O. Uspenskaya, B. Vellas, P. J. Visser, M. Wagner; Subjective Cognitive Decline Initiative (SCD-I) Working Group, A conceptual framework for research on subjective cognitive decline in preclinical Alzheimer's disease. *Alzheimers Dement.* **10**, 844–852 (2014).
63. O. Hansson, S. Lehmann, M. Otto, H. Zetterberg, P. Lewczuk, Advantages and disadvantages of the use of the CSF Amyloid β (Aβ) 42/40 ratio in the diagnosis of Alzheimer's Disease. *Alzheimers Res. Ther.* **11**, 34 (2019).
64. M. L. Gorno-Tempini, A. E. Hillis, S. Weintraub, A. Kertesz, M. Mendez, S. F. Cappa, J. M. Ogar, J. D. Rohrer, S. Black, B. F. Boeve, F. Manes, N. F. Dronkers, R. Vandenberghe, K. Rascovsky, K. Patterson, B. L. Miller, D. S. Knopman, J. R. Hodges, M. M. Mesulam, M. Grossman, Classification of primary progressive aphasia and its variants. *Neurology* **76**, 1006–1014 (2011).
65. G. C. Roman, T. K. Tatemichi, T. Erkinjuntti, J. L. Cummings, J. C. Masdeu, J. H. Garcia, L. Amaducci, J.-M. Orgogozo, A. Brun, A. Hofman, D. M. Moody, M. D. O'Brien, T. Yamaguchi, J. Grafman, B. P. Drayer, D. A. Bennett, M. Fisher, J. Ogata, E. Kokmen, F. Bermejo, P. A. Wolf, P. B. Gorelick, K. L. Bick, A. K. Pajeau, M. A. Bell, C. DeCarli, A. Culebras, A. D. Korczyn, J. Bogousslavsky, A. Hartmann, P. Scheinberg, Vascular dementia: Diagnostic criteria for research studies. Report of the NINDS-AIREN International Workshop. *Neurology* **43**, 250–260 (1993).
66. S. J. Crutch, J. M. Schott, G. D. Rabinovici, M. Murray, J. S. Snowden, W. M. van der Flier, B. C. Dickerson, R. Vandenberghe, S. Ahmed, T. H. Bak, B. F. Boeve, C. Butler, S. F. Cappa, M. Ceccaldi, L. C. de Souza, B. Dubois, O. Felician, D. Galasko, J. Graff-Radford, N. R. Graff-Radford, P. R. Hof, P. Krolak-Salmon, M. Lehmann, E. Magnin, M. F. Mendez, P. J. Nestor, C. U. Onyike, V. S. Pelak, Y. Pijnenburg, S. Primativo, M. N. Rossor, N. S. Ryan, P. Scheltens, T. J. Shakespeare, A. Suárez González, D. F. Tang-Wai, K. X. X. Yong, M. Carrillo, N. C. Fox; Alzheimer's Association ISTAART Atypical Alzheimer's Disease and Associated Syndromes Professional Interest Area, Consensus classification of posterior cortical atrophy. *Alzheimers Dement.* **13**, 870–884 (2017).
67. I. G. McKeith, D. W. Dickson, J. Lowe, M. Emre, J. T. O'Brien, H. Feldman, J. Cummings, J. E. Duda, C. Lippa, E. K. Perry, D. Aarsland, H. Arai, C. G. Ballard, B. Boeve, D. J. Burn, D. Costa, T. del Ser, B. Dubois, D. Galasko, S. Gauthier, C. G. Goetz, E. Gomez-Tortosa, G. Halliday, L. A. Hansen, J. Hardy, T. Iwatsubo, R. N. Kalaria, D. Kaufer, R. A. Kenny, A. Korczyn, K. Kosaka, V. M. Y. Lee, A. Lees, I. Litvan, E. Londos, O. L. Lopez, S. Minoshima, Y. Mizuno, J. A. Molina, E. B. Mukaetova-Ladinska, F. Pasquier, R. H. Perry, J. B. Schulz, J. Q. Trojanowski, M. Yamada; for the Consortium on DLB, Diagnosis and management of dementia with Lewy bodies: Third report of the DLB Consortium. *Neurology* **65**, 1863–1872 (2005).
68. P. Nirmalraj, R. Lehner, D. Thompson, B. Rothen-Rutishauser, M. Mayer, Subcellular imaging of liquid silicone coated-intestinal epithelial cells. *Sci. Rep.* **8**, 10763 (2018).
69. I. Usov, R. Mezzenga, FiberApp: An open-source software for tracking and analyzing polymers, filaments, biomacromolecules, and fibrous objects. *Macromolecules* **48**, 1269–1280 (2015).
70. E. Kozlova, A. Chernysh, V. Moroz, V. Sergunova, O. Gudkova, E. Manchenko, Morphology, membrane nanostructure and stiffness for quality assessment of packed red blood cells. *Sci. Rep.* **7**, 7846 (2017).
71. G. Ciasca, M. Papi, S. di Claudio, M. Chiarpotto, V. Palmieri, G. Maulucci, G. Nocca, C. Rossi, M. de Spirito, Mapping viscoelastic properties of healthy and pathological red blood cells at the nanoscale level. *Nanoscale* **7**, 17030–17037 (2015).
72. M. S. Albert, S. DeKosky, D. Dickson, B. Dubois, H. H. Feldman, N. C. Fox, A. Gamst, D. M. Holtzman, W. J. Jagust, R. C. Petersen, P. J. Snyder, M. C. Carrillo, B. Thies, C. H. Phelps, The diagnosis of mild cognitive impairment due to Alzheimer's disease: Recommendations from the National Institute on Aging-Alzheimer's Association workgroups on diagnostic guidelines for Alzheimer's disease. *Alzheimers Dement.* **7**, 270–279 (2011).

Acknowledgments: P.N.N. thanks M. Calame and A. Dommann for strategic support. T.S. and A.F. thank S. Zimmerer, G. Toller, B. Wagner, C. Achtnich, A. Müller, and M. Velicky for support in the clinical care of patients, data collection, and blood smear preparation. T.S. and A.F. also thank B. Tettenborn for strategic support. **Funding:** We acknowledge the Empa-KSSG research grant (number: 21/11) for financial support. **Author contributions:** P.N.N. and A.F. conceived the study. P.N.N. performed AFM measurements and data analysis. A.F. and T.S. recruited the patients and collected the clinical data. P.N.N., T.S., and A.F. jointly performed the statistical analysis and data interpretation. P.N.N. wrote the manuscript, and all authors contributed to editing and revising the manuscript. **Competing interests:** The authors declare that they have no competing interests. **Data and materials availability:** All data needed to evaluate the conclusions in the paper are present in the paper and/or the Supplementary Materials.

Submitted 27 April 2021
Accepted 4 August 2021
Published 24 September 2021
10.1126/sciadv.abj2137

Citation: P. N. Nirmalraj, T. Schneider, A. Felbecker, Spatial organization of protein aggregates on red blood cells as physical biomarkers of Alzheimer's disease pathology. *Sci. Adv.* **7**, eabj2137 (2021).

ScienceAdvances

Spatial organization of protein aggregates on red blood cells as physical biomarkers of Alzheimer's disease pathology

Peter Niraj NirmalrajThomas SchneiderAnsgar Felbecker

Sci. Adv., 7 (39), eabj2137.